Surface terracing on ferritic stainless steel fibres and potential relevance to in-vitro cel growth

Athina Emmanuel Markaki, Kevin M Knowles, Rachel A. Oliver, Ali Gholinia

Surface terracing on ferritic stainless steel fibres and potential relevance to in-vitro cel growth

Journal:	*Philosophical Magazine & Philosophical Magazine Letters*
Manuscript ID:	TPHM-09-Apr-0139.R1
Journal Selection:	Philosophical Magazine
Date Submitted by the Author:	12-May-2009
Complete List of Authors:	Markaki, Athina; University of Cambridge, Department of Engineering Knowles, Kevin; University of Cambridge, Department of Materials Science and Metallurgy Oliver, Rachel; University of Cambridge, Department of Materials Science and Metallurgy Gholinia, Ali; University of Manchester, Materials Science Centre
Keywords:	EBSD, stainless steels
Keywords (user supplied):	cell growth, fibres, surface energy

Surface terracing on ferritic stainless-steel fibres and potential relevance to *in-vitro* cell growth

Athina E. Markaki[§1], *Kevin M. Knowles*[†], *Rachel A. Oliver*[†], *Ali Gholinia*[*]

[§] University of Cambridge, Department of Engineering, Trumpington Street, Cambridge CB2 1PZ, UK

[†] University of Cambridge Department of Materials Science & Metallurgy, Pembroke Street, Cambridge CB2 3QZ, UK

[*] Oxford Instruments HKL, Majsmarken 1, Hobro, DK 9500, Denmark; now at University of Manchester, Materials Science Centre, Grosvenor Street, Manchester M1 7HS.

1 Corresponding author: Tel: +44 1223 766417; Fax: +44 1223 332662; E-mail address: am253@cam.ac.uk

Keywords: EBSD; fibres; stainless steel; surface energy; cell growth

Abstract

Since many natural and biological materials are cellular, often with relatively high porosity levels (although sometimes these pores are partly filled with a fluid or a soft and compliant solid in the natural state), various types of porous materials are of interest for biological applications. A key feature for such applications is the space afforded for invasion first by cells and ultimately by osseous tissue and vasculature. The surface should be chemically and topologically suitable for cells to penetrate and interlock. There is evidence that fine scale topographic features can affect both the adhesion and ingrowth of cells. One way of creating topographic features, such as terraces, is to employ suitable heat treatments so as to expose preferentially the low surface energy crystallographic planes via surface diffusion. In the present work, the topography and crystallography of surface terraces, generated on solid-state-sintered ferritic stainless-steel fibre networks, have been characterized by electron back-scattered diffraction, atomic force microscopy and scanning electron microscopy. Initial work on the effect of these fine scale topographic features on cell proliferation shows encouraging results.

1. Introduction

There is current research interest in highly porous, permeable, foamed metals. While casting or powder production routes are commonly used to produce metals in this form, bonded fibre networks also have certain attractions. The properties of such networks can be

largely controlled by tailoring the fibre characteristics (material, diameter and sectional shape) and the network architecture (volume fraction, orientation distribution and inter-joint spacing). Potential applications for these bonded fibre networks include filters [1-3], preforms for composite production [4], electrodes for fuel cells and batteries[5, 6], sandwich panel cores [7, 8], acoustic damping modules [9], heat exchangers [10, 11] and biomedical devices [12, 13].

For networks based on fibres of ferromagnetic materials, such as ferritic stainless steels, it has been proposed that applications could be developed involving magnetic actuation, an example being the stimulation of bone growth via the application of a magnetic field [14, 15]. Key features to this type of application are the optimisation of the network architecture and the fibre surfaces being chemically and topologically suited for ingrowth of bone cells. For example, it is known that the pore size best suited to promote bone cell ingrowth is ~100-300 μm [16], a size which is readily achievable for a fibre network. Ferritic stainless steels generally exhibit good biocompatibility [17, 18], but there remains a need to create an optimal surface topography. As a result, there is extensive research on the effect of surface topography on cell attachment and proliferation, e.g.[19-23]. Surface patterning techniques such as dry etching, photolithography, and electron beam lithography are often applied to flat surfaces in order to generate fine scale topographic features. However, while these techniques are capable of sub-micron resolution, they tend to be slow, cumbersome, expensive and difficult to apply to large areas or three-dimensional surfaces. An attractive and inexpensive route to creating topographic features such as terraces on surfaces is by means of a heat treatment, leading to the preferential exposure of low energy crystallographic planes via (surface) diffusion. There is considerable scope for tailoring such features in order to optimise cell adhesion and proliferation. The present paper is concerned with surface terraces induced during the solid-state heat treatment of ferritic -steel fibres. Information is presented concerning the topography and crystallographic orientation of these terraces, together with some initial results on their effect on cell growth.

2. Experimental procedures

2.1 Material production

2.1.1 Single fibres

The fibres, supplied by FibreTech Ltd (Nottingham, UK), were made from 446 ferritic stainless steel, with a composition of Fe–26wt%Cr–1.5wt%Mn–1wt%Si–0.12wt%C. ~~melt-spun to lengths of 20 mm~~. They were produced by direct solidification from the melt by casting onto a large, water-cooled Cu-alloy rotating wheel, with precisely machined surface patterns. The surface morphology, sectional shape and microstructure of these fibres, in the

as-received condition, are shown in Fig. 1. As is apparent from this figure, the sectional area varies somewhat along the length of the fibres, having the approximate shape of a crescent. The average equivalent diameter of each fibre was measured to be 60 ±10 μm. The columnar dendritic solidification structure emanating from the protrusions of the Cu-alloy rotating wheel in the as-produced fibres is evident in Fig. 1(c).

2.1.2 Solid-state sintered mats

Fibre mats were produced by solid-state sintering of fibre networks at the Fraunhofer Institute for Manufacturing Technology and Applied Materials Research in Germany (IFAM Dresden) and at Fibretech Ltd. in the U.K. These mats contained ~ 15 vol% of 446 fibres, melt-spun to lengths of 20 and 5 mm respectively. A secondary electron scanning electron micrograph of a fibre mat in plan view produced at IFAM Dresden is shown in Fig. 2.

The two thermal histories applied to the fibre networks are shown in Fig. 3. Heat treatment HT1 was carried out at IFAM Dresden using a vacuum furnace set at a pressure of 5.5×10^{-5} mbar. Heat treatment HT2 was performed at Fibretech Ltd. using a vacuum furnace set at a pressure of 3×10^{-3} mbar.

2.2 Microstructural characterisation

2.2.1 Scanning electron microscopy and electron back-scattered diffraction

Microstructural examination of polished and etched cross-sections of fibres was performed in secondary electron mode using a JEOL 5800 scanning electron microscope. Compositional analysis was performed using energy dispersive X-ray spectroscopy (EDS).

Information on the crystallographic orientation of surface terraces was obtained using electron back-scattered diffraction (EBSD). EBSD investigations were carried out with a Leo Supra 55 VP Field Emission Gun Scanning Electron Microscope (FEG-SEM) equipped with the Channel 5 EBSD system (Oxford Instruments HKL A/S) and a Nordlys II EBSD detector.

2.2.2 Electrolytic etching and tint etching for optical microscopy

Electrolytic etching, using a 10% aqueous solution of oxalic acid, was used to etch fibres in the as-received condition. Tint etching, with Beraha's reagent (100 mL water, 15 mL HCl, 1 g $K_2S_2O_5$), was used to colour the grains of the heat-treated fibres. This etchant deposits a sulphide-based film that creates colour in bright-field illumination through interference effects. The colour was enhanced by using polarized light during the reflected light optical microscopy.

2.2.3 Atomic force microscopy

The surface topography of the fibres subjected to the HT1 heat treatment was investigated using a Veeco Dimension 3100 Atomic Force Microscope (AFM), in intermittent contact (IC) mode. Veeco RTESP silicon probes were used for all AFM characterisation. Fibres were aligned approximately perpendicular to the AFM fast-scan direction. The diameter of the fibres was larger than the scan distance chosen for observation.

2.3 Cell culture studies

2.4.1 Cell culture and seeding

Bovine cartilage cells (chondrocytes) were isolated from the metacarpophalangeal joints of 18-month-old steers. Porous fibre scaffolds were prepared from sintered fibre mats by waterjet cutting. The scaffolds were disk-shaped with a diameter of 10 mm and a thickness of about 1.2 mm. Before culture, the scaffolds were cleaned ultrasonically in acetone for 5 min, ethanol for 5 min and finally in distilled water for another 5 min. They were then autoclaved at 134 °C for 1 hour.

The isolated cells were seeded at a density of 10^4 per scaffold sample. In order to enhance cell incorporation, each sample was placed onto a hydrophobic polytetrafluoroethylene (PTFE) membrane (5 μm pore size). The samples were incubated at 37 °C in a 5% CO_2 atmosphere and saturated humidity for 3.5 hours to allow for cell attachment. After this period, the samples were each placed in a well of a 24-well plate, covered with 1 ml of culture medium and incubated for a total of 19 days. The culture medium was Dulbecco's modified Eagle's medium (DMEM), supplemented with 10 vol% Fetal Bovine Serum (FBS), and 1 vol% antibiotics containing 10,000 international units (IU) per ml of penicillin and 10 mg per ml of streptomycin.

2.4.2 Cell growth

Changes in cell growth were monitored using the AlamarBlue assay. This assay incorporates a redox indicator dye, AlamarBlue. The seeded scaffolds were incubated for 4 hours with fresh culture medium supplemented with 10 vol% AlamarBlue dye. A total of 10 replicates were used for each scaffold. In the presence of metabolically active cells, the redox indicator exhibits a change from oxidised (non-fluorescent, blue) form to reduced (fluorescent, red) form. Following incubation, 100 μL medium from each well was transferred to a 96-well microplate and replicated 3 times. Fluorescence (excitation 530 nm, emission 590 nm) was measured on a Fluostar Optima microplate reader.

The AlamarBlue reduction by cartilage cells expressed as fluorescence emission intensity units was measured on days 1, 4, 6, 8, 11, 13, 15 and 19 of the culture period for different networks. The % reduction of AlamarBlue for each case was calculated using the formula [24]

$$\%\ \text{reduction of AlamarBlue} = \frac{S_{AB}^{x} - S_{AB}^{control}}{S_{AB}^{100\%\ reduced} - S_{AB}^{control}}$$

where S_{AB}^{x} is the AlamarBlue fluorescence signal of the sample at day x, $S_{AB}^{100\%\ reduced}$ is the signal of the 100% reduced form of AlamarBlue and $S_{AB}^{control}$ is the signal from the control: the culture medium supplemented with 10 vol.% AlamarBlue dye. The 100% reduced form of AlamarBlue was produced by autoclaving controls (ie. culture medium supplemented with 10 vol.% AlamarBlue dye) at 121°C for 15 minutes.

2.4.3 Cellular Morphology

For scanning electron microscopy (SEM) observations, the cell-seeded samples were 'fixed' with 4% glutaraldehyde and then rinsed three times with phosphate buffered saline. The samples were then dehydrated in a graded ethanol series (ethanol acts as a cryo-protectant). They were incubated in 100% ethanol, frozen in liquid nitrogen, and afterwards broken. Critical point drying was then carried out. The samples were sputtered with gold before being examined in a JEOL 5800 scanning electron microscope.

3. Microstructural development

3.1 Phase constitution and grain structure

A comparison of Fig. 1(c) and Fig. 4 shows that heat treatment HT1 leads to coarsening of the grain size of the ferritic stainless steel from a few μm to a few tens of μm and the formation of relatively coarse precipitates at grain boundaries and within individual grains. EDS analysis showed that these precipitates are Cr-rich $(Cr, Fe)_{23}C_6$ carbides. Isothermal sections of the Fe-Cr-C ternary phase diagram for the carbon content concerned [25], suggest that these carbides are thermodynamically stable below 1100ºC. This implies that the $(Cr, Fe)_{23}C_6$ carbides are not present during the HT1 (or HT2) temperature hold, but are formed during the subsequent slow cooling of 3ºC/min (Fig. 3).

A fibre after heat treatment HT2 is shown in Fig. 5. It can be seen that there are no carbide particles in this SEM micrograph. Furthermore, substantial grain coarsening has occurred, creating a 'bamboo' structure with a grain size slightly larger than the fibre diameter.

3.2 Surface Terracing and Crystallographic Orientation

3.2.1 Topographic Features

SEM images of HT1 heat-treated samples often revealed surface terraces of the type shown in Fig. 6. The orientation of these terraces varies between grains, but is systematic within a particular grain, in a way that suggests they are dependent on crystallographic orientation. Furthermore, it is apparent from this figure that the $(Cr, Fe)_{23}C_6$ carbides are also faceted.

AFM data from the surface of an HT1 heat-treated fibre are shown in Fig. 7. The features revealed are consistent with the SEM micrographs (Fig. 6). In order to measure the relative heights of the terraces seen in Fig. 7(c), a single terrace was selected and a plane-fitting routine was used so that the selected terrace lay within a single horizontal plane. A line profile across the plane-fitted image gave the data in Fig. 7(d), from which the heights and widths of the different terrace steps and also the angle between terrace flanks and steps can be inferred. Global average values were estimated at 605 ± 130 nm and 125 ± 45 nm respectively for the width of the terraces and the height of the terrace steps from the regions chosen for observation. It is also clear from Fig.7(c) that both the "flanks" and the "steps" of these terraces tend to exhibit a consistent orientation, reinforcing the concept of these surfaces representing preferentially-exposed crystallographic planes. The angle between terrace flanks and steps was estimated to be 19 ± 3º. Terracing of a similar scale has recently been observed by scanning tunnelling microscopy [26, 27] in 304L austenitic stainless steel after ultra high vacuum firing at 1300 K for 10–15 min. In these studies the terraces were interpreted as {111} planes of the cubic close-packed austenite because they were able to observe monatomic steps within these terraces of 0.21 nm height, while the 125 ± 45 nm wide steps between terraces were interpreted as {100} and {110} planes, i.e., planes which, relative to other planes in cubic close-packed crystal structures, have low surface energies, as can be shown from density functional theory calculations on other metals with cubic close-packed crystal structures [28]. However, while it might be tempting to interpret the surface reconstruction in the heat-treated fibres in terms of faceting into low energy planes on the basis of the AFM observations alone, AFM does not directly provide sufficient crystallographic information to make this interpretation with confidence, particularly in the absence of monoatomic terraces. Instead, EBSD was used to extract crystallographic data on the terraces.

3.2.2 Crystallography of Terraces (EBSD)

The advantage of EBSD as a characterisation technique is that crystallographic information can be obtained from individual grains of materials [29]. In practice, the orientation of relatively large (25-100 μm) planar surfaces such as facets seen on fracture

surfaces have been determined experimentally by SEM using a photogrammetric technique in which ideally the coordinates in projection of three points defining a plane are determined at different angles of tilt [30-37]. For the terracing seen on the fibres here, their small size would have made this procedure prone to error. The procedure adopted instead was to obtain crystallographic information on the grain orientation at two different tilts using EBSD and then combine this with additional specimen tilting in the microscope without the EBSD detector in place to obtain images of the projected area of a terrace as a function of specimen tilt. However, EBSD can only determine the indices of planes constituting features such as terraces directly if the normal to the features is within the EBSD detector range of angles. This is actually a very stringent condition experimentally: the solid angle of EBSD patterns subtended at the specimen is of the order of 20-25°. Furthermore, it is not uncommon in current EBSD systems for the sample tilt relative to the electron beam to be fixed on a specially tilted specimen stage at 70° towards the detector capturing the EBSD image and for there to be no ability to rotate the sample *in situ* given the limitations on specimen–detector geometry imposed by EBSD.

The scanning electron microscope system used in this work was able to rotate the specimen into position for the EBSD work and take EBSD patterns from individual grains at tilt values of 55° and 70° relative to a known tilting axis within the scanning electron microscope. Analysis of these EBSD patterns then enabled prediction of the grain orientations at other values of tilt where it was not possible to bring in the EBSD detector for confirmation of the grain orientation, both because the signal would be too weak and also because the geometry within the scanning electron microscope would prevent the detector from being moved into position.

This procedure does not enable a unique identification of surface features because the crystallographic information is specific to grains, rather than surface features. However, as the specimen is tilted in a systematic manner, the projected area of a particular feature seen in SEM images on the surfaces of individual grains will alter in a systematic manner, and will be at a maximum when the normal to the feature is parallel to the electron beam. When the normal is close to the electron beam, the projected area will be close to the maximum possible, varying as cos θ, where θ is the angle between the electron beam and the normal to the feature under consideration.

The principle of the methodology used in this work is illustrated by data shown in Figs. 8 and 9. Output from the Channel 5 EBSD system produced orientational data for each grain at the EBSD tilt setting examined (55° or 70°) in the form of inverse pole figures specifying the horizontal X_O direction, the vertical Y_O direction and the normal Z_O to the plane of the SEM image using stereographic projection geometry.

A pole in a particular pole figure could then be specified in terms of a normalised direction [*UVW*] within a standard 001 – 101 – 111 stereographic triangle where

$$U = \cos\theta \sin\phi$$

$$V = \sin\theta \sin\phi$$

$$W = \cos\phi$$

in which θ is the angle shown in the Y_O inverse pole figure for the 70° tilt setting in Fig. 8 and ϕ is determined from the condition $r/R_s = \tan\phi/2$, where R_s is the radius of the stereogram (i.e., of the projection sphere) and r is also shown in the Y_O inverse pole figure for the 70° tilt setting in Fig. 8. This procedure therefore produced unit vectors [*UVW*] specifying the directions X_O, Y_O and Z_O seen on the image with respect to the crystal axes of the grain under observation. An orthogonal set specifying X_O, Y_O and Z_O was then determined by choosing X_O to be within the standard 001 – 101 – 111 stereographic triangle and permuting the [*UVW*] values for Y_O and Z_O to produce a set of vectors which were almost orthogonal, typically to within 0.2°, but not exactly orthogonal because of measurement errors. However, within the measurement errors, two of three vectors could be manipulated to be exactly orthogonal, with respect to which the third vector could be specified as the vector product of these two orthogonal vectors. Therefore, at the end of procedure, a set of orthonormal vectors specifying X_O, Y_O and Z_O for the 55° and 70° tilt settings could be produced. These two sets of orthonormal vectors form columns of matrices which were termed *R*70 and *R*55 for the two tilt settings. Thus, for example, *R*70 for point 2 in Fig. 8(a) was

$$R70 = \begin{bmatrix} 0.62468 & -0.27420 & 0.73115 \\ 0.06699 & -0.91495 & -0.40003 \\ 0.77800 & 0.29887 & -0.55262 \end{bmatrix}$$

while for point 2 on Fig. 8(b), *R*55 was

$$R55 = \begin{bmatrix} 0.58854 & -0.09691 & 0.80264 \\ 0.01116 & -0.99172 & -0.12793 \\ 0.80839 & 0.08425 & -0.58259 \end{bmatrix}$$

reflecting the fact that the rotation between the SEM micrographs in Fig. 8(a) and Fig. 8(b) is, to within experimental error, around the X_O axis. In this case the rotation matrix describing the rotation $R70.R55^{-1}$ between the images seen in Fig. 8(a) and Fig. 8(b) was determined to be an angle of 16.71° about the direction [–0.74291, 0.12268, –0.65806], i.e., an angle close to the expected 15° about an axis reasonably close to the crystallographic directions determined for X_O at these two orientations. In this particular case, the points selected for

EBSD analysis at 55° and 70° tilt were sufficiently far apart for there to have been low angle boundary rotations to explain why the angular agreement was not better than 1.71°. Subsequent experiments on other fibres showed that angular accuracies were improved significantly if the area selected for EBSD analysis was the same (within experimental error) at both tilt settings.

For subsequent calculations, it was assumed in this particular example that *R*70 was correct and that the tilt axis and sense of rotation away from this setting was correct, so that the orientation of the normal Z_O to the plane of the SEM image could be determined for other tilt settings where the EBSD detector could not be used. Examples of images from the grains shown in Fig. 8 at other tilt settings are shown in Fig. 9. For the left hand grain, the orientation of Z_O at the four tilt settings shown in Fig. 9 was:

$$Z_{O,40^\circ} = \begin{bmatrix} 0.82147 \\ 0.09565 \\ -0.56217 \end{bmatrix}, \quad Z_{O,25^\circ} = \begin{bmatrix} 0.80083 \\ 0.33944 \\ -0.49342 \end{bmatrix}, \quad Z_{O,10^\circ} = \begin{bmatrix} 0.73718 \\ 0.55819 \\ -0.38078 \end{bmatrix}, \quad Z_{O,0^\circ} = \begin{bmatrix} 0.67289 \\ 0.68264 \\ -0.28500 \end{bmatrix}$$

It is apparent from Figs 8 and 9 that, as the specimen is rotated, the normal to terrace A in Fig. 9 is most close to Z_O at the 25° tilt setting. A consideration of the possible terrace orientations in the light of the tilt experiments shows that the normal to terrace A is $[2\bar{1}1]$, 6.4° from the orientation of Z_O at the 25° tilt setting. As the specimen rotates away from this tilt setting, towards higher or lower tilt settings, the projected area of terrace A decreases. Furthermore, it is also obvious from an examination of the whole image that terrace A is most close to being viewed end-on at the 25° tilt setting. Similar considerations, given information about Z_O at the various tilt angles, suggest that the normal to terrace B is $[10\bar{1}]$ and the normal to terrace C is $[2\bar{1}\bar{1}]$. Hence these three terraces are {101} and {211} planes. A similar analysis for the grain in Figs. 8 and 9 from which EBSD data was obtained as point 1 also shows that the terrace labelled E can be labelled as a $(10\bar{1})$ terrace, D a $(2\bar{1}\bar{1})$ terrace and F a $(2\bar{1}1)$ terrace.

That the terrace steps shown in Figs. 8 and 9 have been indexed as {011} and {211} planes is perhaps not surprising. Such planes correspond to low energy crystallographic planes, according to Wulff's construction [28, 38]. For both the b.c.c. metals Fe and Cr, the surface energies per atom follow the sequence $\sigma_{110} < \sigma_{100} < \sigma_{211} < \sigma_{310} < \sigma_{111}$. For pure iron [38], it has been shown that $\sigma_{111} < \sigma_{321} < \sigma_{210}$ and that the surface energy increases with surface roughness. Per unit area it is still the case that {110} surfaces have lower free energies than other surfaces. It is therefore entirely reasonable that this sequence will hold for the b.c.c. phase present in this Fe-Cr alloy and that the facets seen will reflect (a) the local macroscopic (unfaceted) normal to the surface and (b) the relative surface energies per atom.

Further EBSD work corroborated the observation that {110} terraces were common on the surfaces of the wires and a qualitative re-examination of the terraces shown in Fig. 6 shows that {110} and {211} facets can be readily identified from their characteristic terrace morphologies. In this context, it is relevant that the angle between a (110) terrace and its four nearest {321} planes is 19.11°, the angle between this terrace and its two nearest {210} planes is 18.43°. These angles would be consistent with the angles determined between terraces and steps in the AFM work and, if these {321} and {210} planes were to be steps, it would help to account for the faceting behaviour of the {110} terraces seen in Figs. 6, 8 and 9.

3.2.3 Mechanism of Terrace Formation

The terracing arises as a result of atomic redistribution, caused by surface diffusion, so as to create a surface structure with a lower free energy. The atmosphere, and hence the presence or absence of a surface (oxide) film, dictates the ease with which these terraces can form. The crystallographic anisotropy of the surface energy of the b.c.c. phase is the driving force, with low surface energy planes tending to be preferentially exposed. If there were an oxide film on the surface, it would most likely be fine-grained or amorphous, and so there would probably be little or no energy gain from exposing particular crystallographic planes. Even if the oxide were large-grained, and had an epitaxial relationship with the matrix, it might well not exhibit much anisotropy of its surface energy. Furthermore, the presence of an oxide film would tend to inhibit surface diffusion of the matrix atoms.

At 1200°C, the native chromium-rich oxide film on the stainless-steel fibre has the chemical equilibrium

$$2\mathrm{Cr} + {}^{3}/_{2}\mathrm{O_2} \quad = \quad \mathrm{Cr_2O_3} \qquad\qquad \Delta G^\circ = -754\ \mathrm{kJ\ mol^{-1}}$$

At equilibrium, $\Delta G = 0$, and so

$$\Delta G^\circ = -RT \ln K = -RT \ln\left(\frac{a_{\mathrm{Cr_2O_3}}}{(a_{\mathrm{Cr}})^2\,(p\mathrm{O_2})^{3/2}} \right)$$

using $a_{\mathrm{Cr_2O_3}} = 1$ and $a_{\mathrm{Cr}} = 0.4$ as typical values appropriate for the activity of chromium oxide and chromium in stainless steel, the equilibrium partial pressure of O_2 at 1200°C is calculated from the above equation to be 10^{-18} atm, i.e., an oxygen partial pressure that can be attained in an Ultra High Vacuum (UHV) system. However, such pressures can also be attained in a good vacuum system if oxygen getters such as titanium granules are used to eliminate the oxygen. Hence, under the vacuum conditions used in HT1, it is likely that the chromium-rich surface oxide film is absent, enabling the surfaces of the fibres to reconstruct during the heat treatment.

4 Cell Culture Studies

4.1 Cell Growth

The percentage reduction of AlamarBlue after different culture times for networks with and without surface terracing on the fibres is shown in Fig. 10. It can be seen that the metabolic activity of the cartilage cells increases with culture time, suggesting that the fibre networks are able to support *in vitro* growth of these cells. Greater AlamarBlue reduction (i.e., higher levels of cell growth) is observed on networks with surface terracing as compared to those without, with cell growth activity on these networks increasing significantly from days 13 to 19. It is worth noting that both fibre networks have the same surface chemistry, a nm-thick Cr_2O_3 film. There are differences in the grain size (see §3.1) and perhaps differences in the film thickness, but both surfaces are expected to be perceived by the cells in a similar way.

4.2 Cellular Morphology and Infiltration

SEM micrographs are shown in Fig. 11 (a) and (b) of round-shaped phenotypic cells (chondrocytes), after 2 days in culture, on fibres with and without surface terracing respectively. In addition, cell edges showing filopodia anchoring onto the fibre surfaces, and secreted fibrous extracellular matrix (ECM) can be seen in Fig. 11(a).

SEM micrographs of sections through fibre network materials are shown in Fig. 11(c) and (d) after 17 days of culture, with and without surface terracing on the fibres respectively. These images suggest that this period was long enough to allow the cells to infiltrate the fibre network materials. They also indicate that cell growth appears to have been more pronounced on the fibres with surface terracing, which is in agreement with the results obtained from the Alamarblue assay (Fig. 10). These observations are encouraging and suggest that a more systematic study should be undertaken to identify the main factors dictating the proliferation and adhesion of cells on these terraced surfaces. To investigate the role of these terraces on cellular behaviour, a range of terrace widths and step heights will be created on flat sheets (rather than fibres, in order to exclude any network architecture effects) by controlling the duration and temperature of the heat treatments.

5 Conclusions

An investigation has been carried out into the topography and crystallographic orientation of surface features produced on ferritic stainless-steel fibres during solid-state sintering, and the effect these surface features have on *in-vitro* cell growth. The following conclusions can be drawn from this work:

Solid-state sintering under suitable vacuum conditions can lead to the exposure of planar, angular surface features (terraces) on ferritic -steel fibres. EBSD analysis and projectional

geometry shows that these terraces correspond to low-index (low surface energy) {110} and {211} crystallographic planes. AFM measurements show that the aspect ratio (height/width) of these terraces is about 5–7, with a step width of several tens of nanometres. The generation of terraces with a crystallographic bias to the exposed surfaces is attributed to surface diffusion stimulated by the crystallographic anisotropy of the surface energy of the b.c.c. phase. While the exact conditions required in order to form such terraces are not yet clear, it can be reasonably assumed that the atmosphere, and hence the presence or absence of a surface (oxide) film, dictates the ease with which these terraces can form.

In vitro cell culture experiments were performed using bovine cartilage cells on fibre networks with and without surface terracing on the fibres. Cell proliferation experiments suggest that networks with surface terracing support higher levels of cell growth over time, with cell growth activity on these networks increasing significantly from days 13 to 19. In addition, observation of the cellular morphology suggests that from the early portion of the culture period, cells on networks with surface terracing secrete significant extracellular matrix.

Acknowledgements

Financial support for AEM and RAO has been provided via an Advanced EPSRC Fellowship and a Royal Society Fellowship respectively. We are particularly grateful to Prof. T.W. Clyne, of the Materials Science Department in Cambridge, for useful discussions. We would also like to thank Olaf Andersen from IFAM Dresden for providing information regarding the HT1 heat treatment, Dr Meera Arumugam of Cambridge University for useful discussions on cell culture, and Lee Marston and Peter Rooney, of Fibretech Ltd, for extensive collaboration and cooperation, including the provision of fibres.

References

1. I. Yuranov, L. Kiwi-Minsker and A. Renken, Applied Catalysis B - Environmental 43 (2003) p.217.
2. M.S.A. Heikkinen and N.H. Harley, Journal of Aerosol Science 31 (2000) p.721.
3. S.H. Kim, C. Sioutas and M.C. Chang, Aerosol Science and Technology 32 (2000) p.197.
4. C. Kaya, A.R. Boccaccini and P.A. Trusty, Journal of the European Ceramic Society 19 (1999) p.2859.
5. S. Ahn and B.J. Tatarchuk, Journal of Applied Electrochemistry 27 (1997) p.9.
6. W.H. Zhu, B.A. Poole, D.R. Cahela et al., Journal of Applied Electrochemistry 33 (2003) p.29.
7. A.E. Markaki and T.W. Clyne, Acta Mater. 51 (2003) p.1341.
8. A.E. Markaki and T.W. Clyne, in *Stainless Steel Sandwich Sheets with Fibrous Metal Cores*, P. Grant, C. Johnston, and B. Cantor eds., Taylor & Francis, 2008, p.149-175.
9. I.O. Golosnoy, J.C. Tan and T.W. Clyne, Adv. Eng. Mater. 10 (2008) p.192.
10. I.O. Golosnoy, A. Cockburn and T.W. Clyne, Adv. Eng. Mater. 10 (2008) p.210.

11. D. Angirasa, Int. J. Heat & Mass Transf. 45 (2002) p.919.
12. F. Walboomers, Y. Paquay and J.A. Jansen, Peritoneal Dialysis International 21 (2001) p.254.
13. J.W. Vehof, M.T. Haus, A.E. de Ruijter et al., Clinical Oral Implants Research 13 (2002) p.94.
14. A.E. Markaki and T.W. Clyne, Biomaterials 25 (2004) p.4805.
15. A.E. Markaki and T.W. Clyne, Acta Mater. 53 (2005) p.877.
16. J.D. Bobyn, R.M. Pilliar, H.U. Cameron et al., Clin. Orth. and Related Research 150 (1980) p.263.
17. M.S. Flores, G. Ciapetti, J.L. Gonzelez-Carrasco et al., J. Mater. Sci: Mater. Med. 15 (2004), p.559.
18. G. Ciapetti, J.L. Gonzelez-Carrasco, L. Savarino et al., Biomaterials 26 (2005) p.849.
19. K. Anselme, P. Linez, M. Bigerelle et al., Biomaterials 21 (2000) p.1567.
20. P. Linez-Bataillon, F. Monchau, M. Bigerelle et al., Biomolecular Engineering 19 (2002) p.133.
21. B.D. Boyan, L.F. Bonewald, E.P. Paschalis et al., Calcified Tissue International 71 (2002) p.519.
22. D.W. Hamilton, K.S. Wong and D.N. Brunette, Calcified Tissue International 78 (2006) p.314.
23. M.J.P. Biggs, R.G. Richards, N. Gadegaard et al., Journal of Orthopaedic Research 25 (2007) p.273.
24. *AlamarBlue™ Technical Datasheet*. 2002, AbD Serotec Ltd.
25. C.V. Doane and J.S. Kirkaldy (Eds.), *Hardenability Concepts with Applications to Steel*, Metallurgical Society of AIME, Pennsylvania, USA, 1978.
26. A. Stupnik and M. Leisch, Vacuum 81 (2007) p.748-751.
27. A. Stupnik and M. Leisch, Vacuum 82 (2008) p.170-173.
28. L. Vitos, A.V. Ruban, H.L. Skriver et al., Surface Science 411 (1998) p.186-202.
29. A.J. Schwartz, M. Kumar and B.L. Adams (Eds.), *Electron Backscatter Diffraction in Materials Science*, Kluwer Academic, New York, 2000.
30. G. Themelis, S. Chikwembani and J. Weertman, Mater. Char. 24 (1990) p.27.
31. D.C. Slavik, J.A. Wert and R.P. Gangloff, J. Mater. Res. 8 (1993) p.2482.
32. V. Randle, J. Mic.(Oxford) 195 (1999) p.226.
33. O. Williams, V. Randle, P. Spellward et al., Mater. Sci. Tech. 16 (2000) p.1372.
34. P.A. Davies and V. Randle, J. Mic.(Oxford) 204 (2001) p.29.
35. Y.J. Ro, S.R. Agnew and R.P. Gangloff, Scr. Mater. 52 (2005) p.531.
36. V. Sinha, M.J. Mills and J.C. Williams, J. Mater. Sci. 42 (2007) p.8334.
37. Y. Ro, S.R. Agnew and R.P. Gangloff, Met. Mater. Trans. A 38 (2007) p.3042.
38. P. Blonski and A. Kiejna, Surface Science 601 (2006) p.123.

Figure Captions

Fig. 1 SEM images of as-received fibres, showing (a) the coarse scale surface morphology, (b) the cross-sectional shape and (c) the dendritic microstructure.

Fig. 2 SEM image of a sintered mat containing 15 vol% of 446 ferritic -steel fibres. The fibres have an average equivalent diameter of 60 μm and were melt-spun to lengths of 20 mm.

Fig. 3 Thermal histories (HT1 and HT2) imposed on the fibre networks.

Fig. 4 Optical micrograph of a polished and tint etched section through sintered fibres subjected to the HT1 heat treatment.

Fig. 5 Scanning electron micrograph of a sintered fibre subjected to the HT2 heat treatment.

Fig. 6 Series of SEM images of fibres, after being subjected to the HT1 heat treatment, taken at increasing magnifications. In (a), artificial colouring has been given to the carbide particles (grey) and the matrix (purple).

Fig. 7 AFM data from the surface of a fibre after the HT1 heat treatment: (a) low magnification amplitude error AFM image, (b) amplitude error AFM image of the region in the white square in (a), (c) topography image of the region in the white square in (b) and (d) Line profile from the AFM data shown in (c) following plane fitting to one of the terraces.

Fig. 8. Inverse pole figures of two sets of data at (a) 70° and (b) 55° tilt settings, together with the corresponding SEM images.

Fig. 9 Scanning electron micrographs at (a) 40°, (b) 25°, (c) 10° and (d) 0° tilt settings.

Fig. 10 Percentage reduction of AlamarBlue after different culture times, for 446 stainless-steel fibre networks with and without terracing.

Fig. 11 (a) and (b) are high magnification SEM images illustrating the attachment of cartilage cells to fibres: (a) with, and (b) without, surface terracing, after two days of culturing. (c) and (d) are low-magnification SEM images showing infiltration of cartilage cells into fibre networks (a) and (b) respectively.

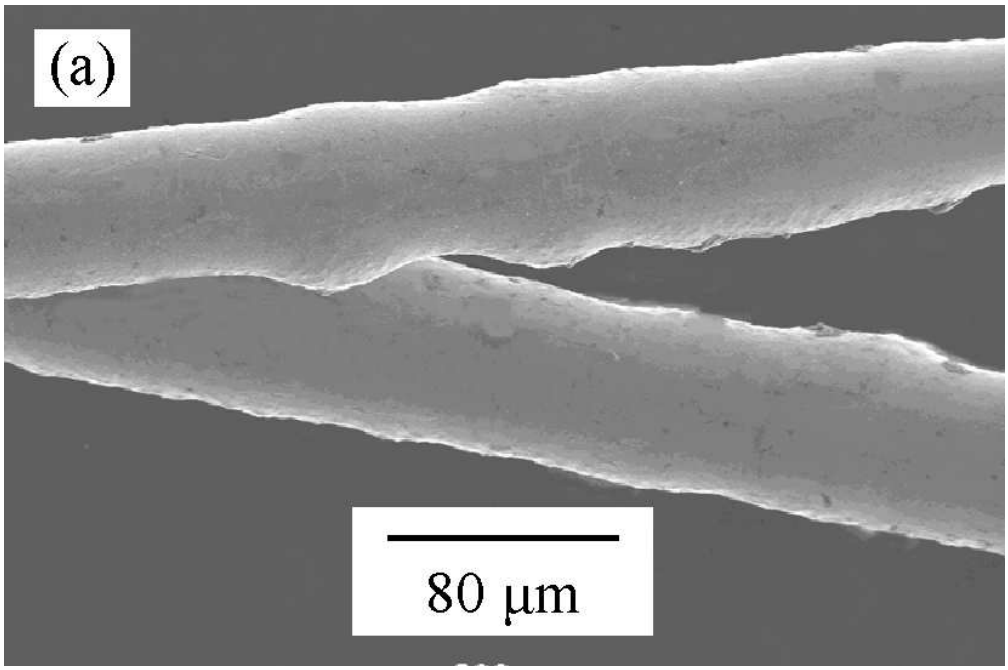

69x46mm (300 x 300 DPI)

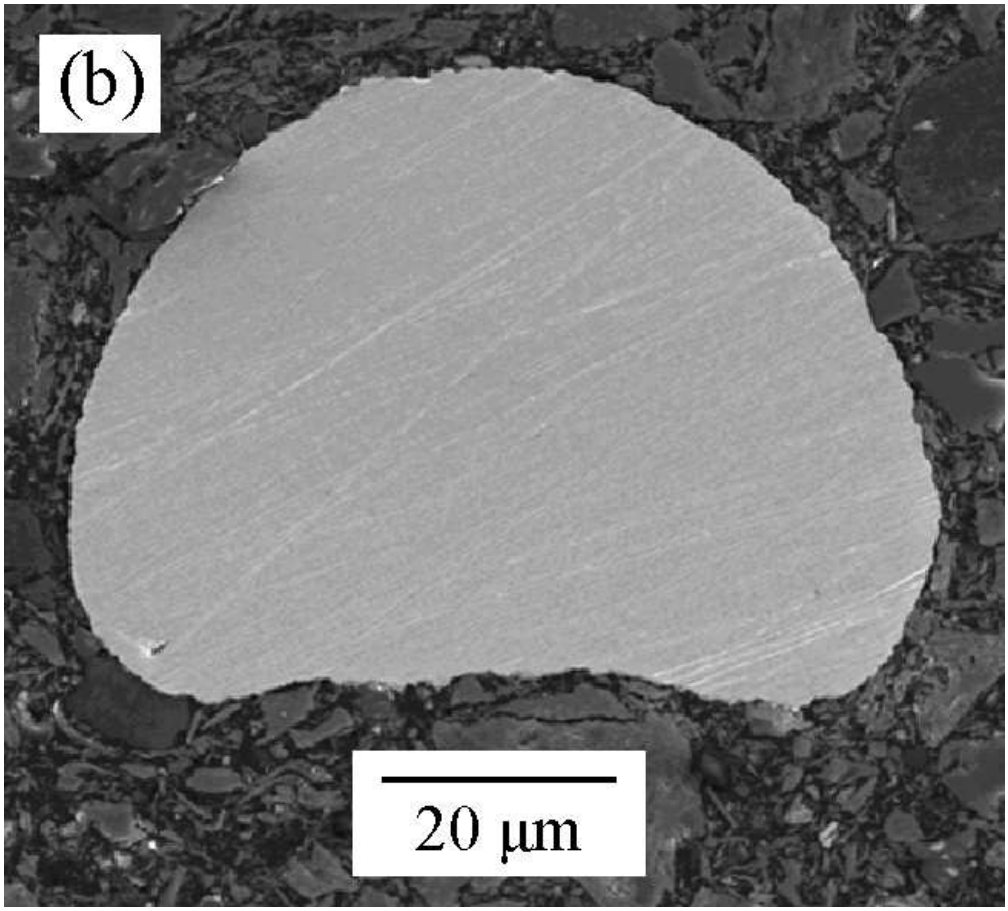

55x49mm (300 x 300 DPI)

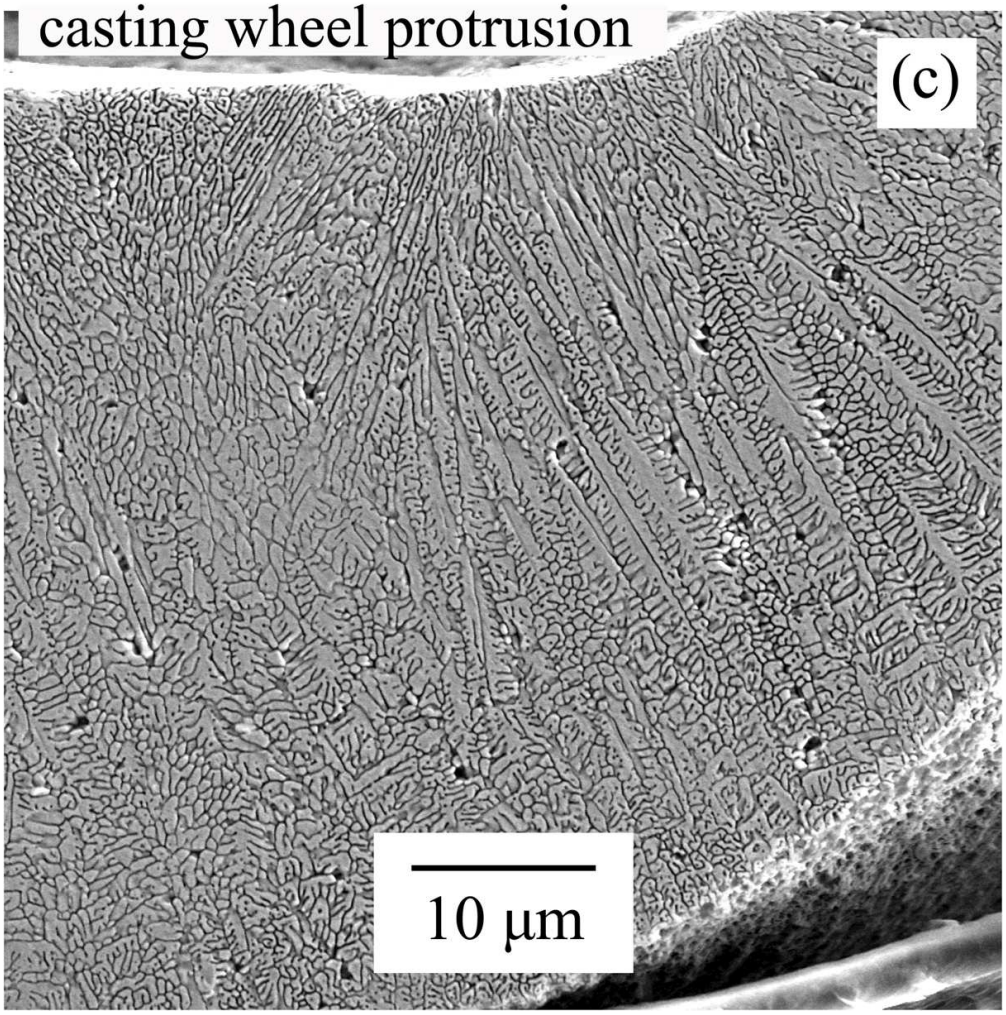

102x103mm (300 x 300 DPI)

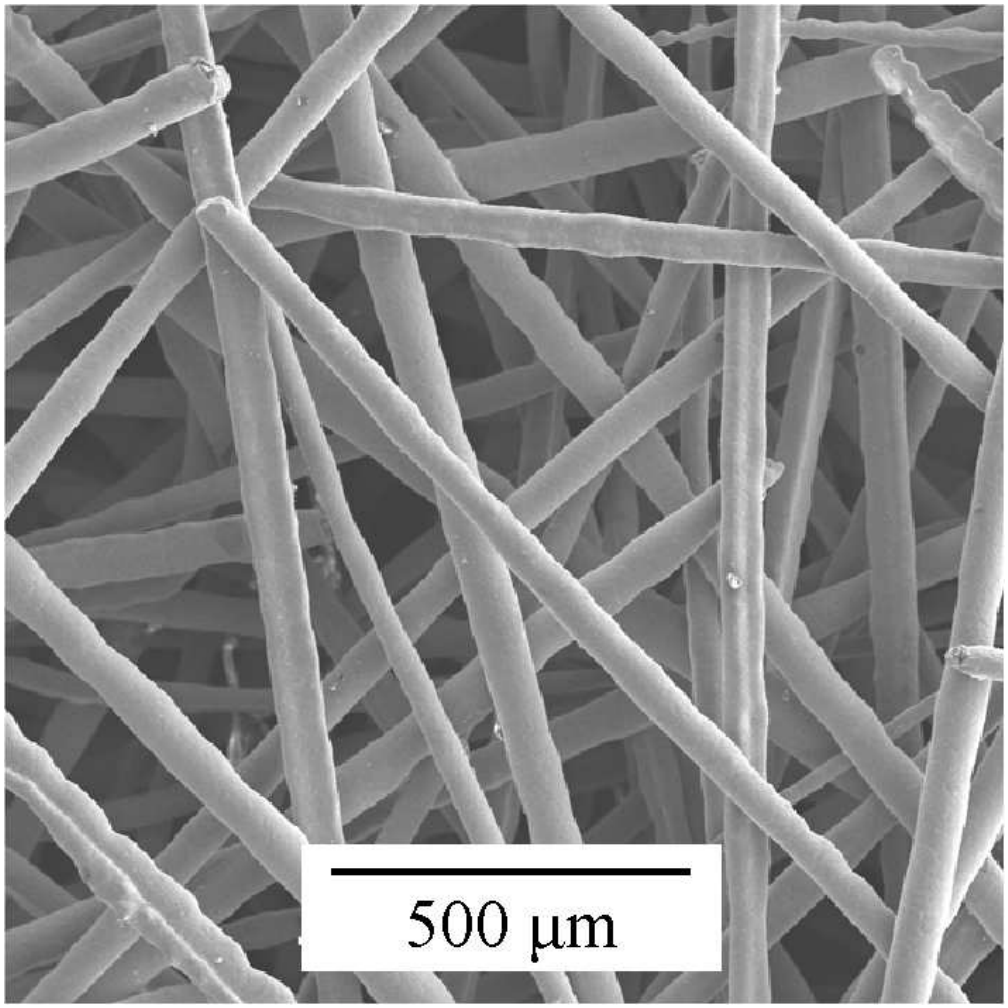

60x60mm (300 x 300 DPI)

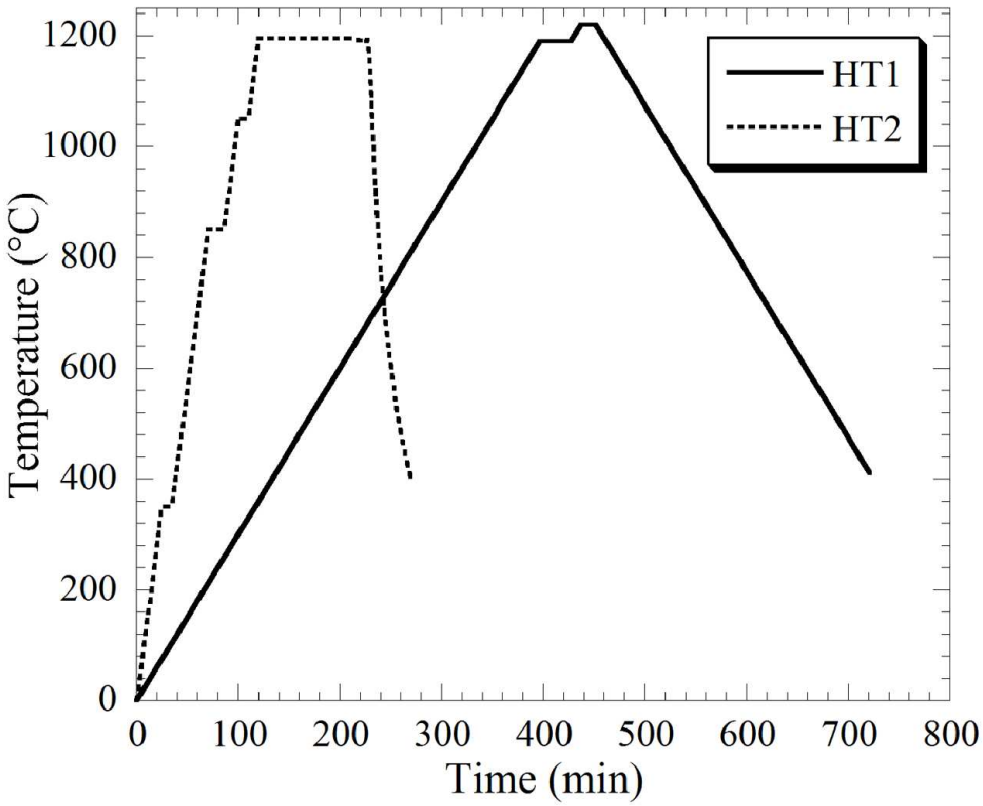

109x94mm (300 x 300 DPI)

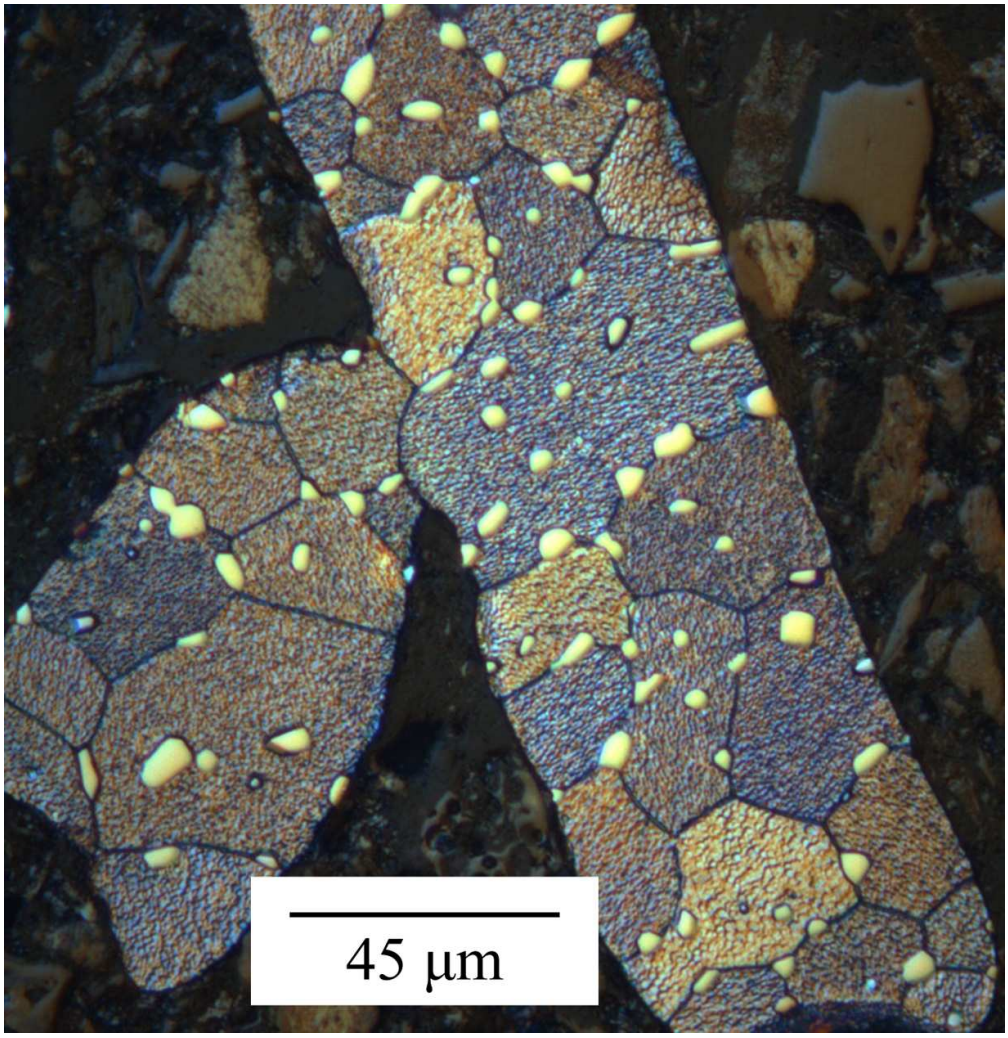

103x106mm (300 x 300 DPI)

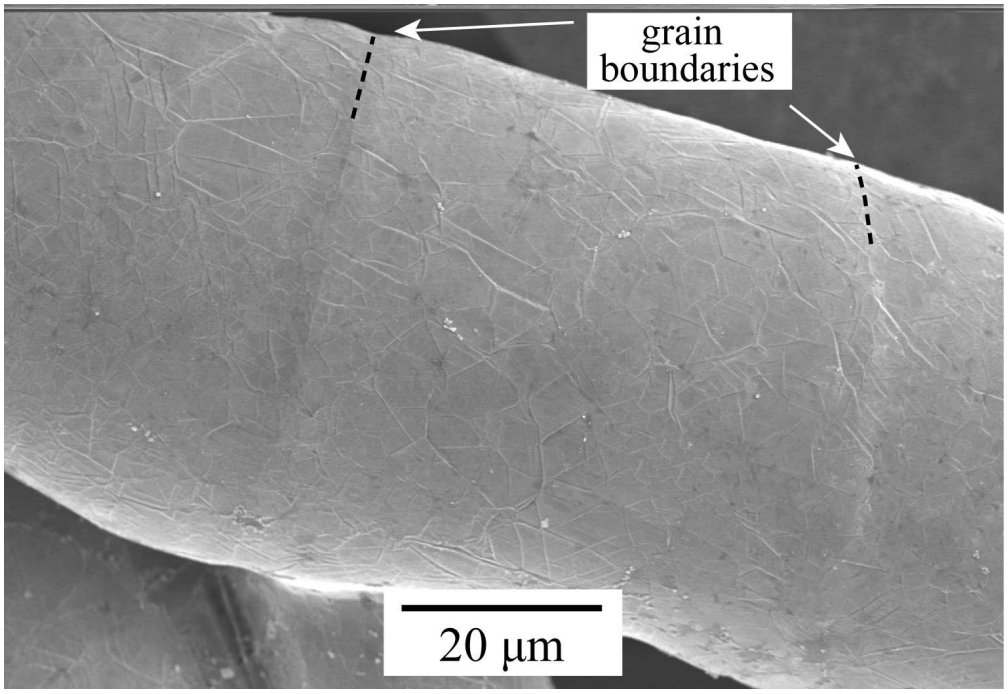

129x88mm (300 x 300 DPI)

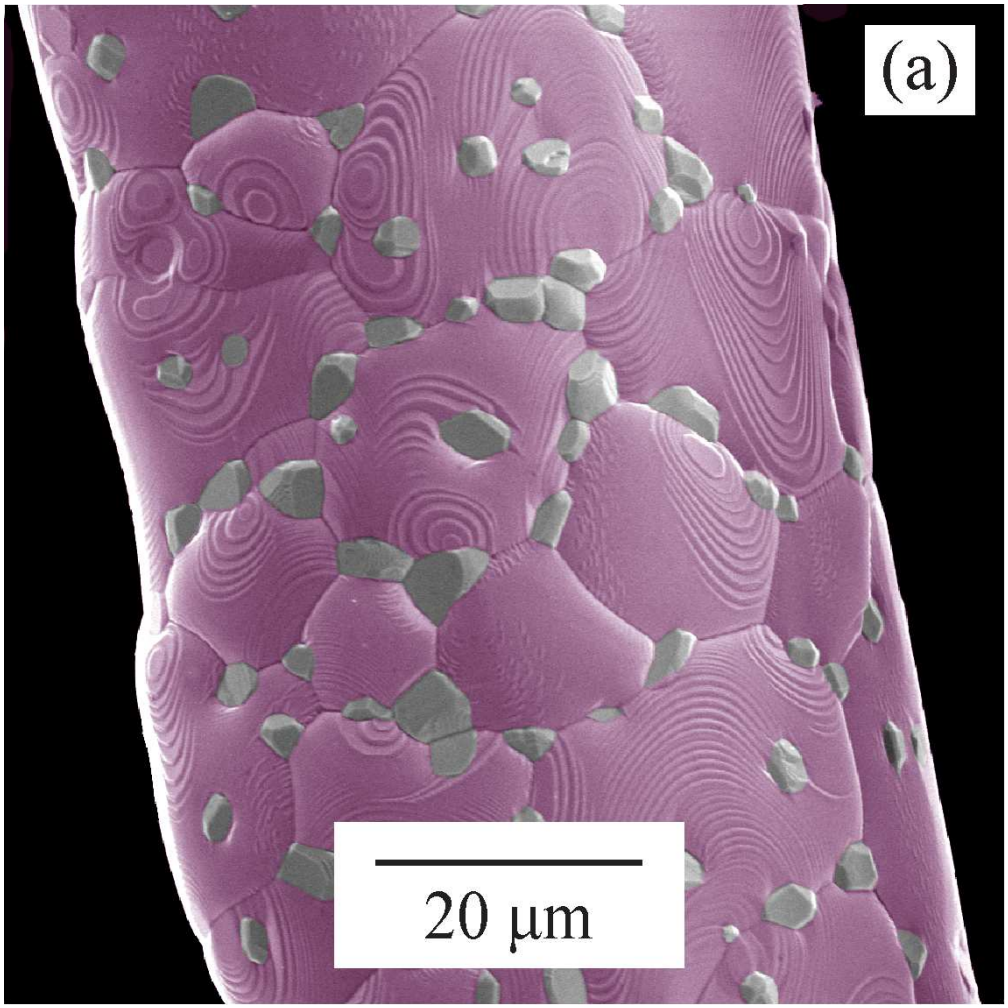

96x96mm (300 x 300 DPI)

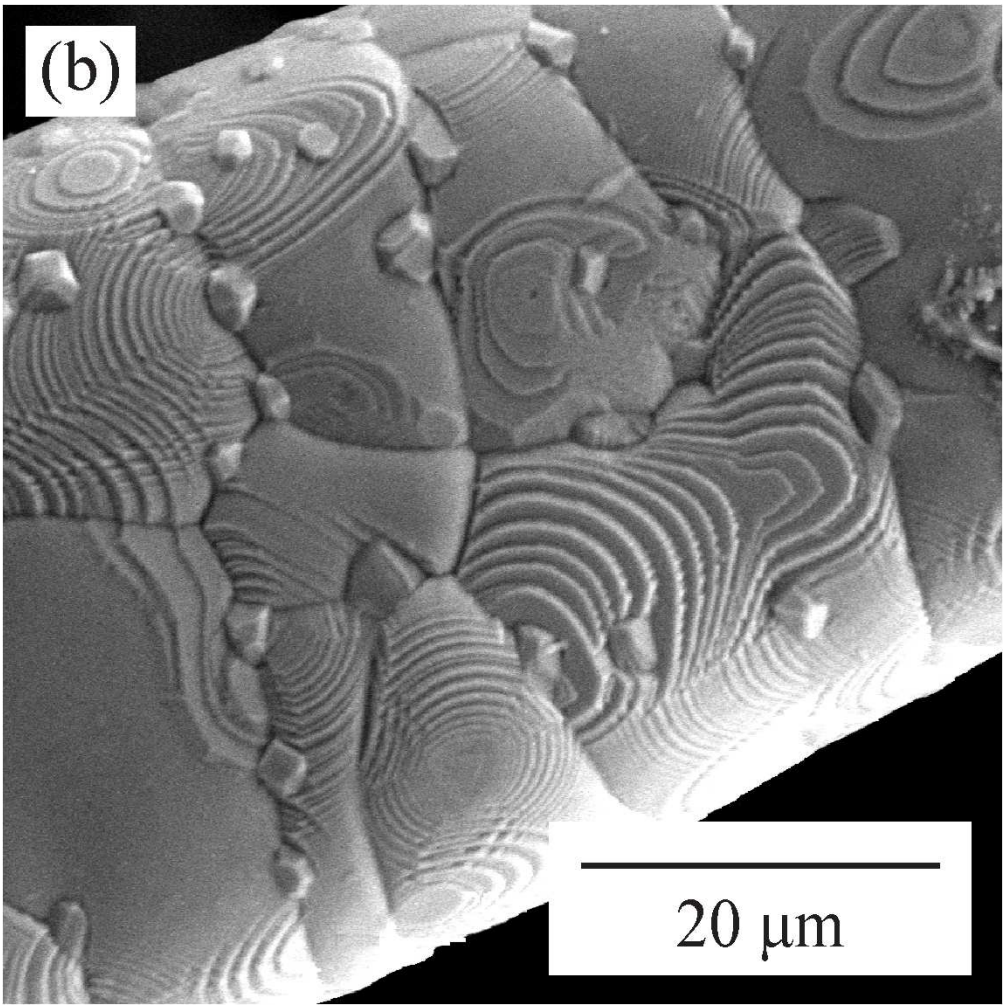

97x97mm (300 x 300 DPI)

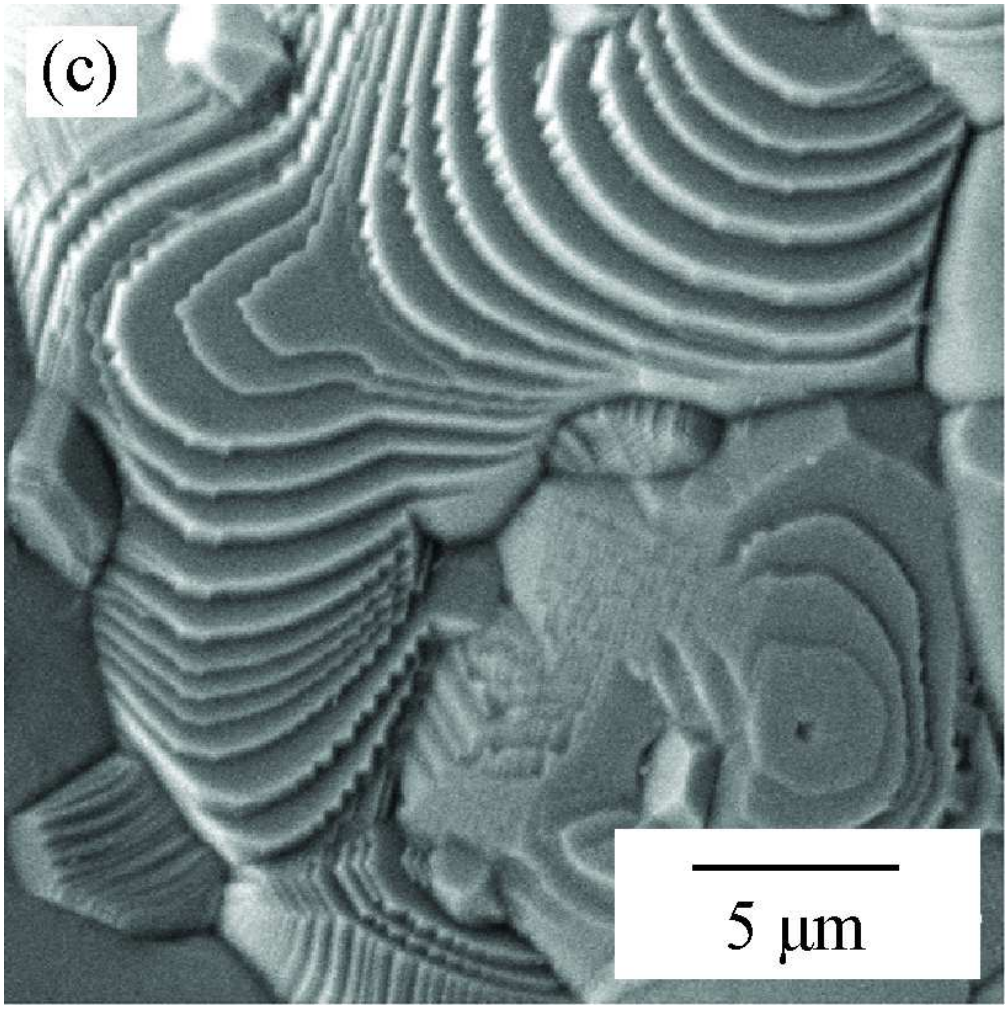

68x68mm (300 x 300 DPI)

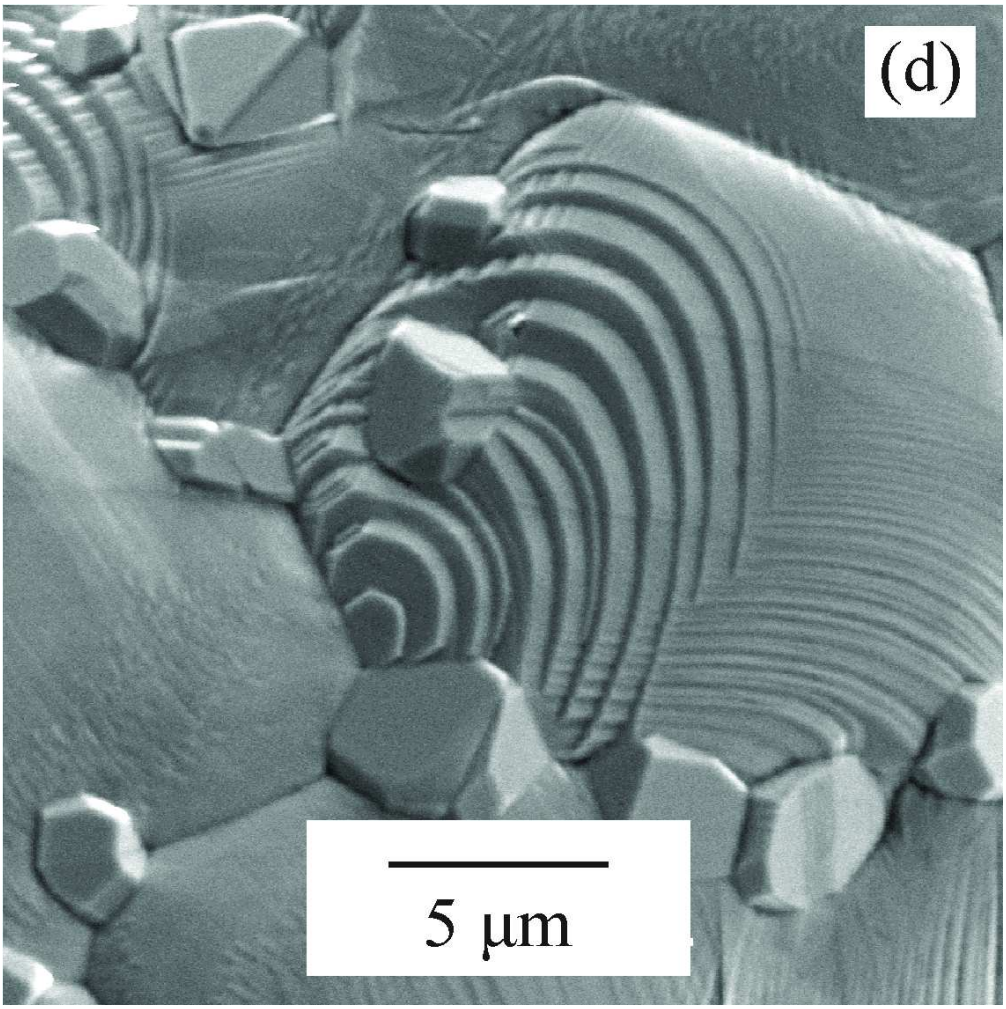

96x96mm (300 x 300 DPI)

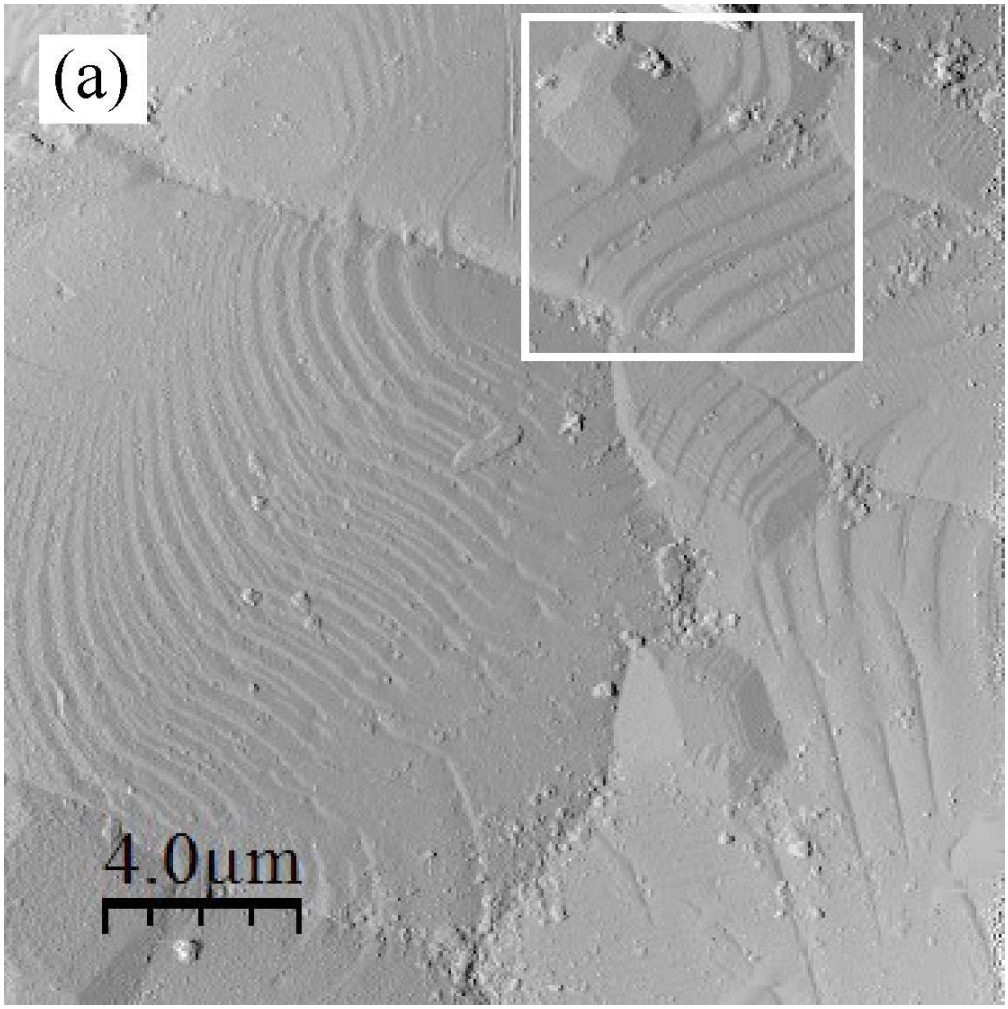

94x94mm (300 x 300 DPI)

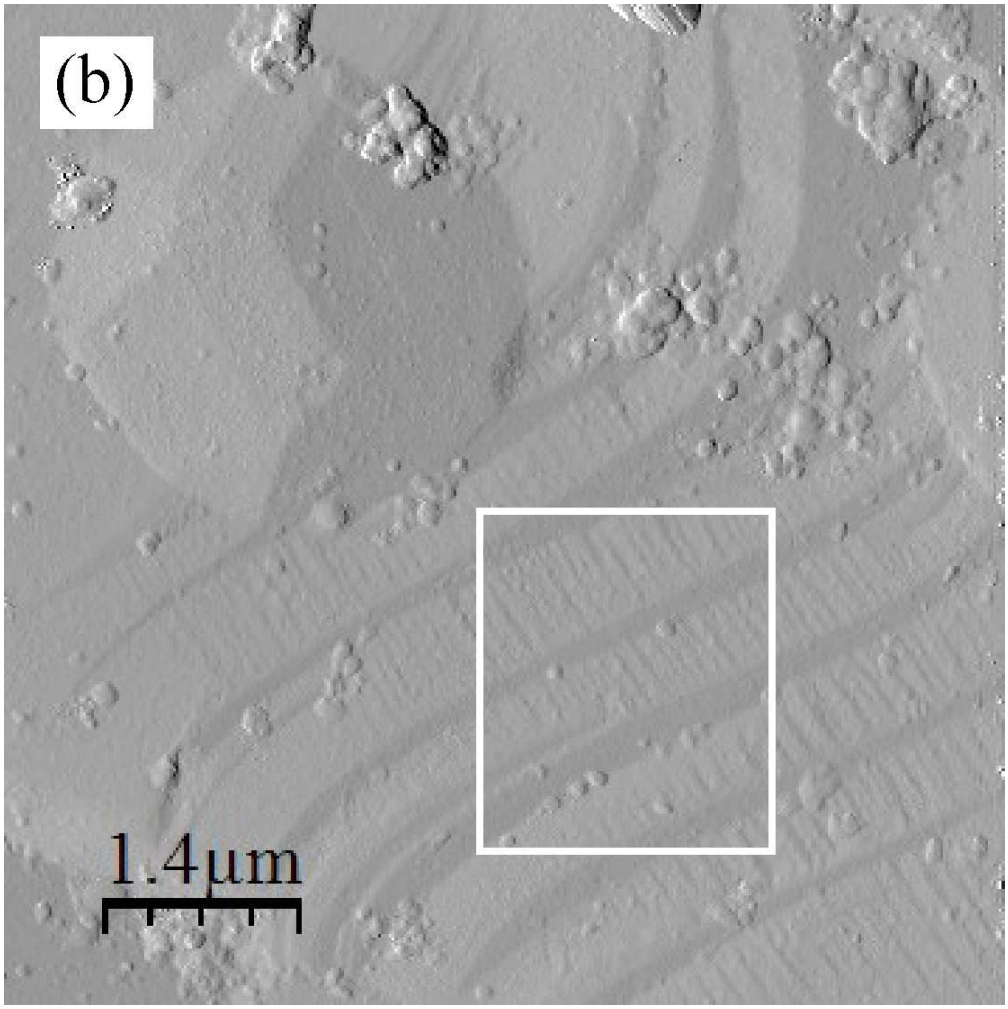

94x94mm (300 x 300 DPI)

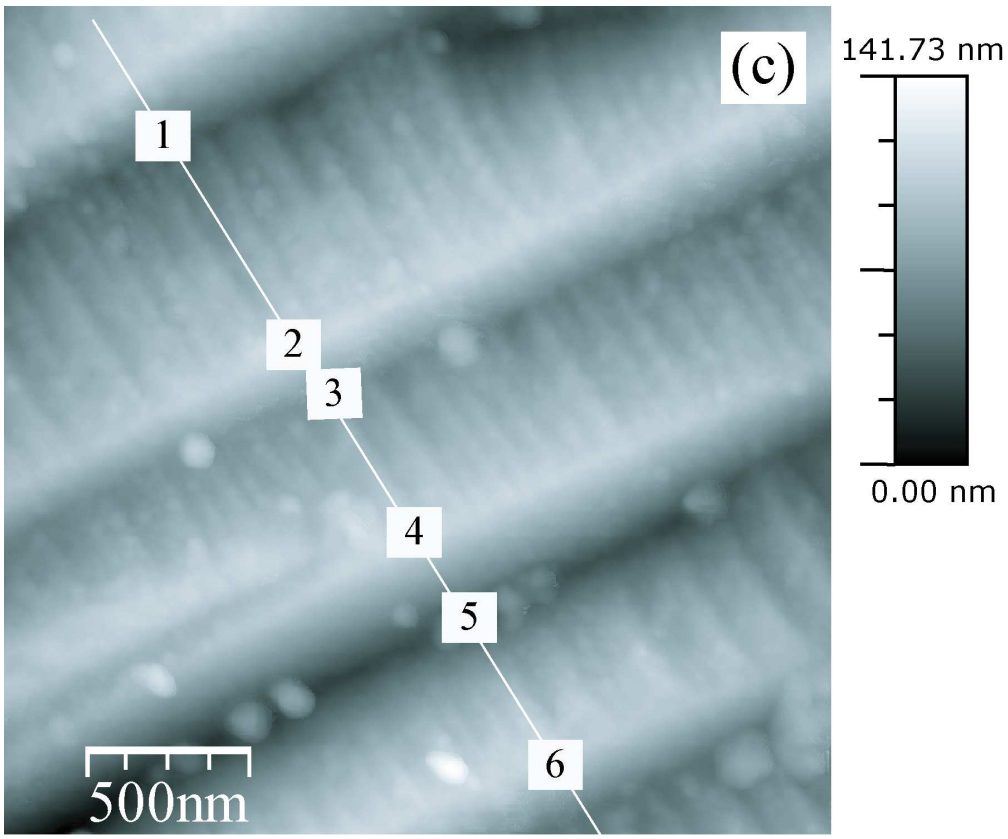

152x127mm (300 x 300 DPI)

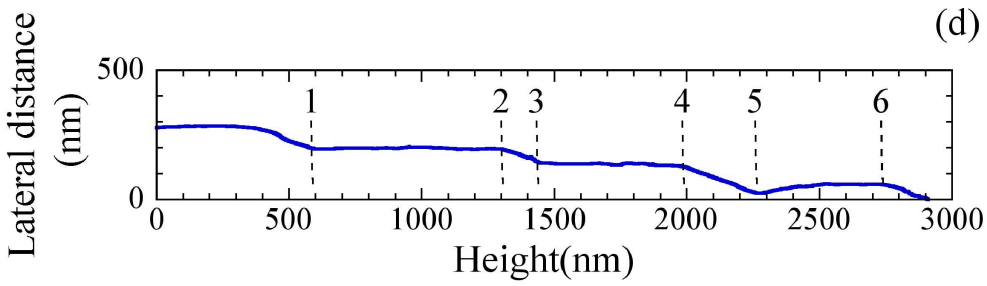

198x59mm (300 x 300 DPI)

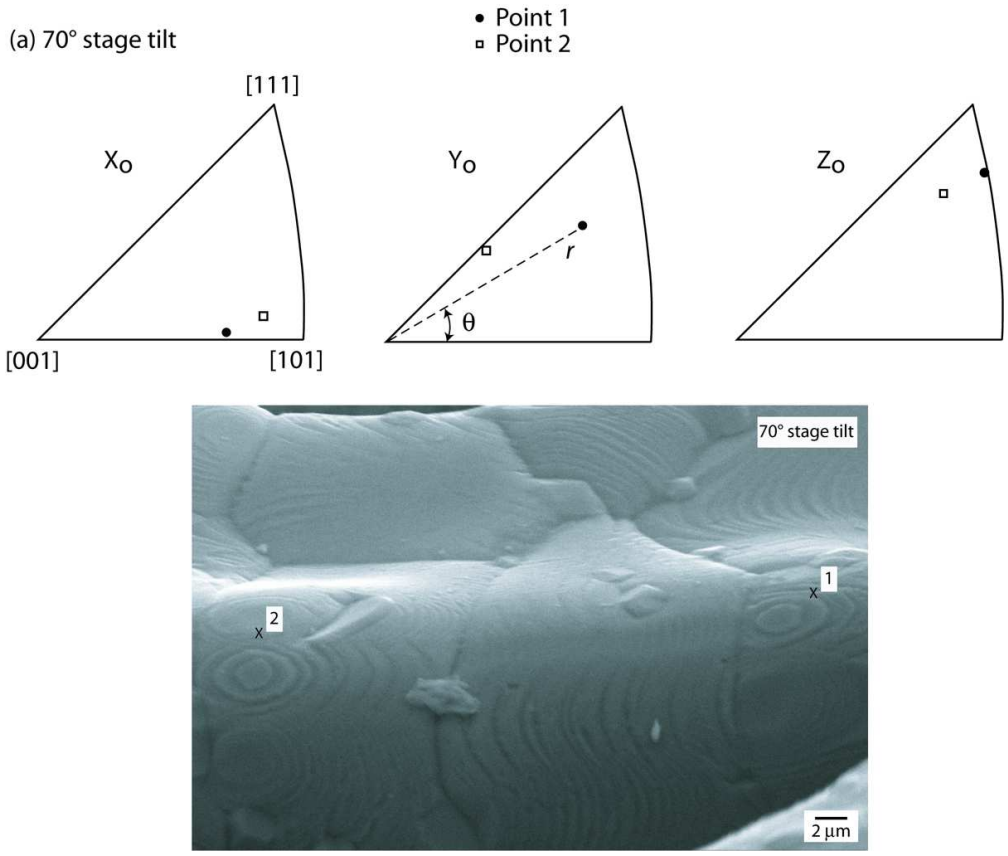

102x86mm (300 x 300 DPI)

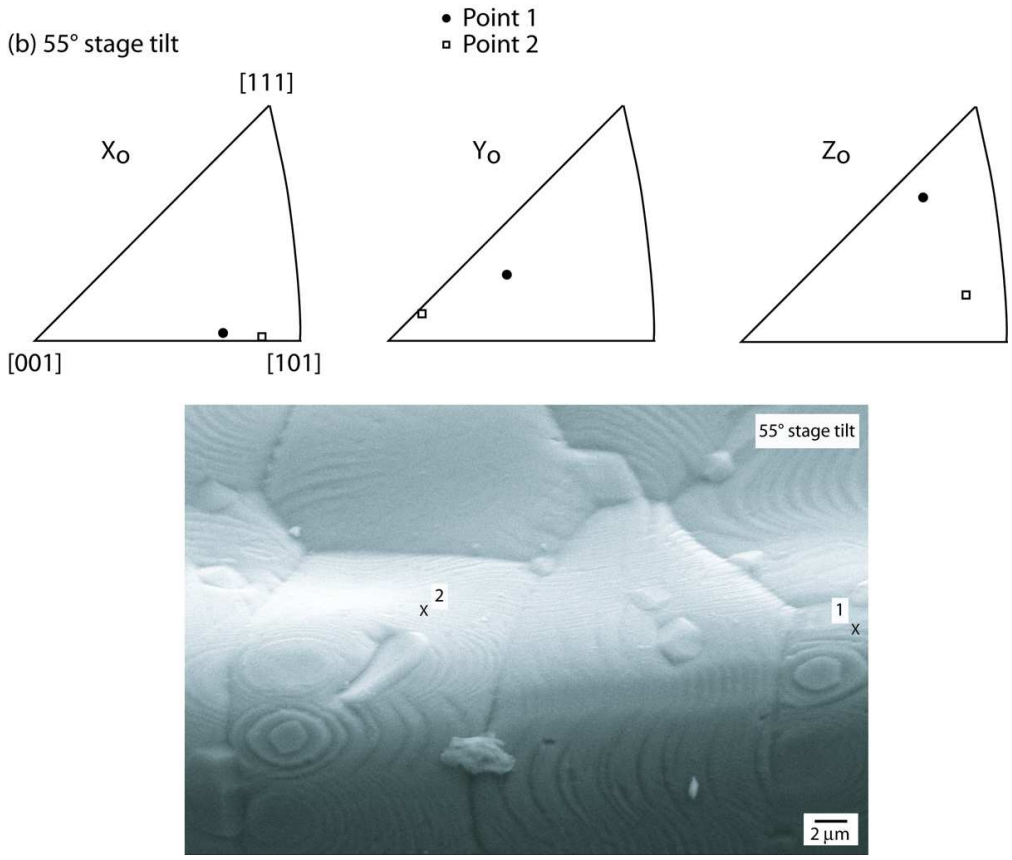

102x86mm (300 x 300 DPI)

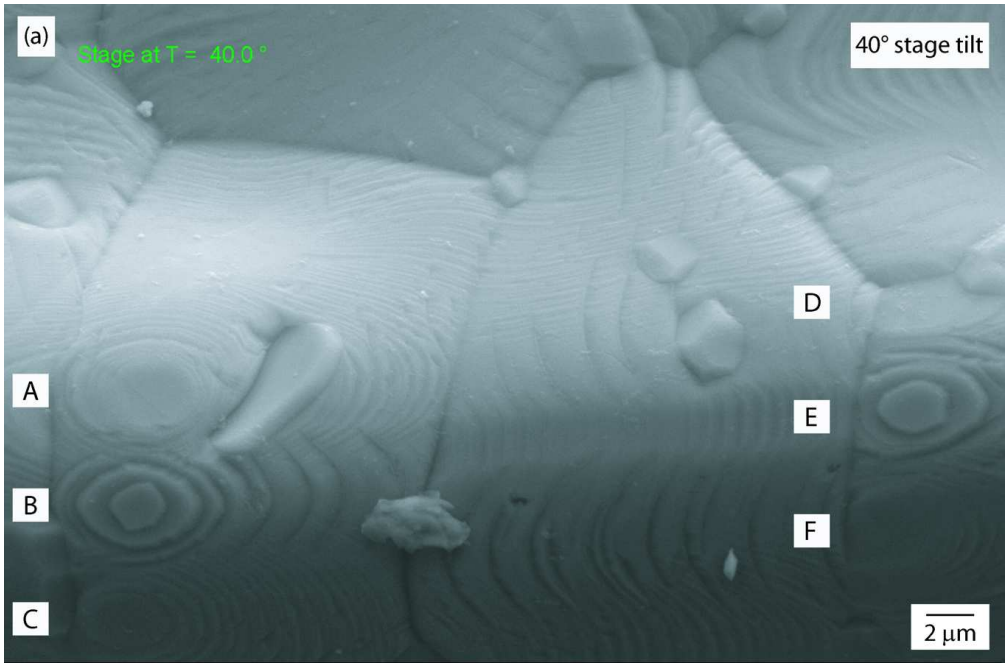

114x75mm (300 x 300 DPI)

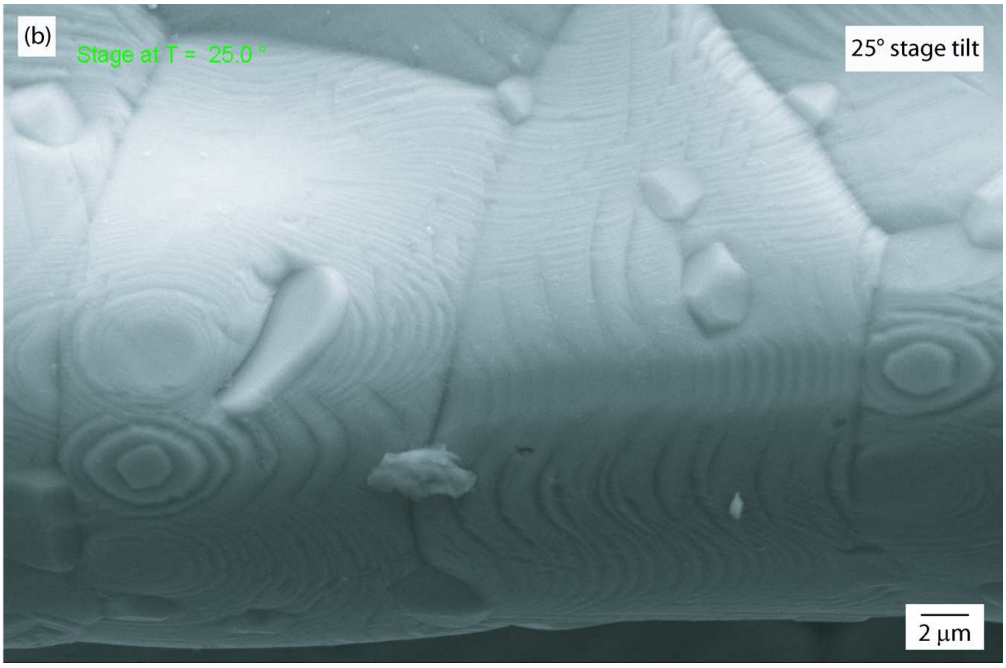

114x75mm (300 x 300 DPI)

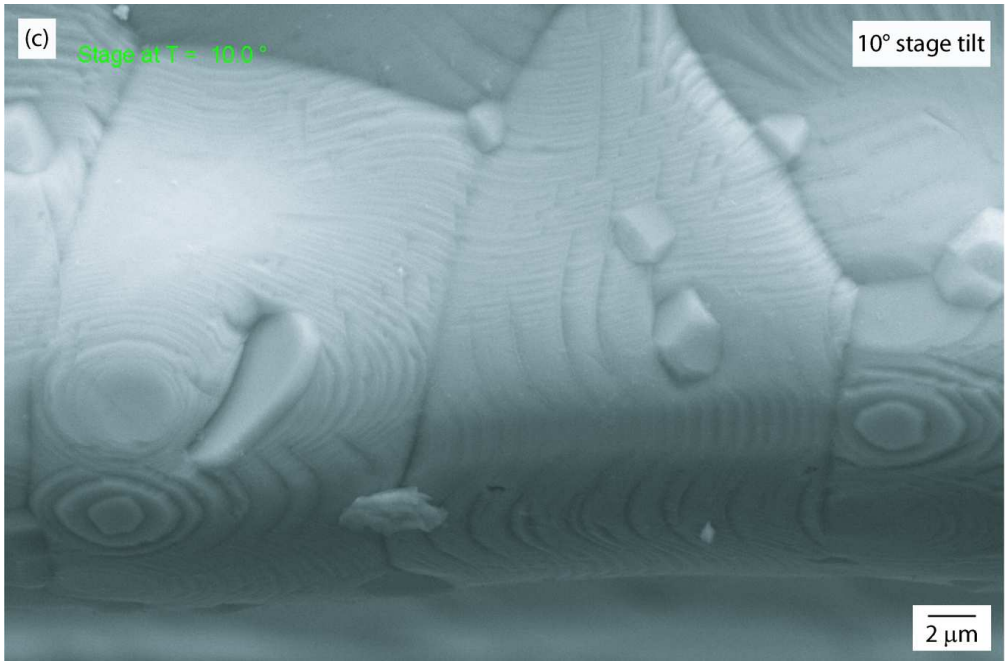

114x75mm (300 x 300 DPI)

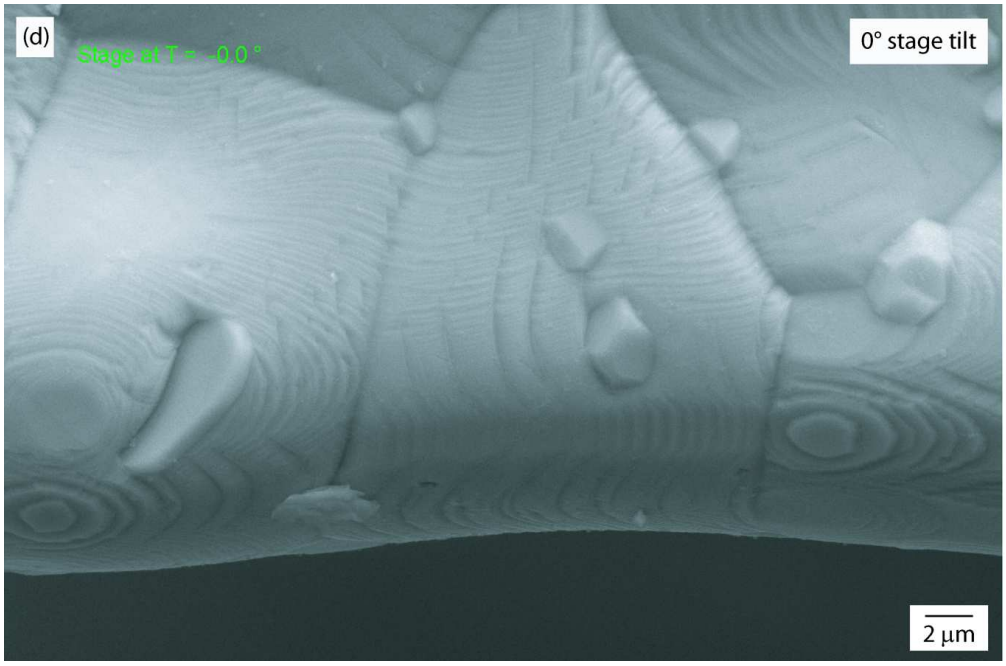

114x75mm (300 x 300 DPI)

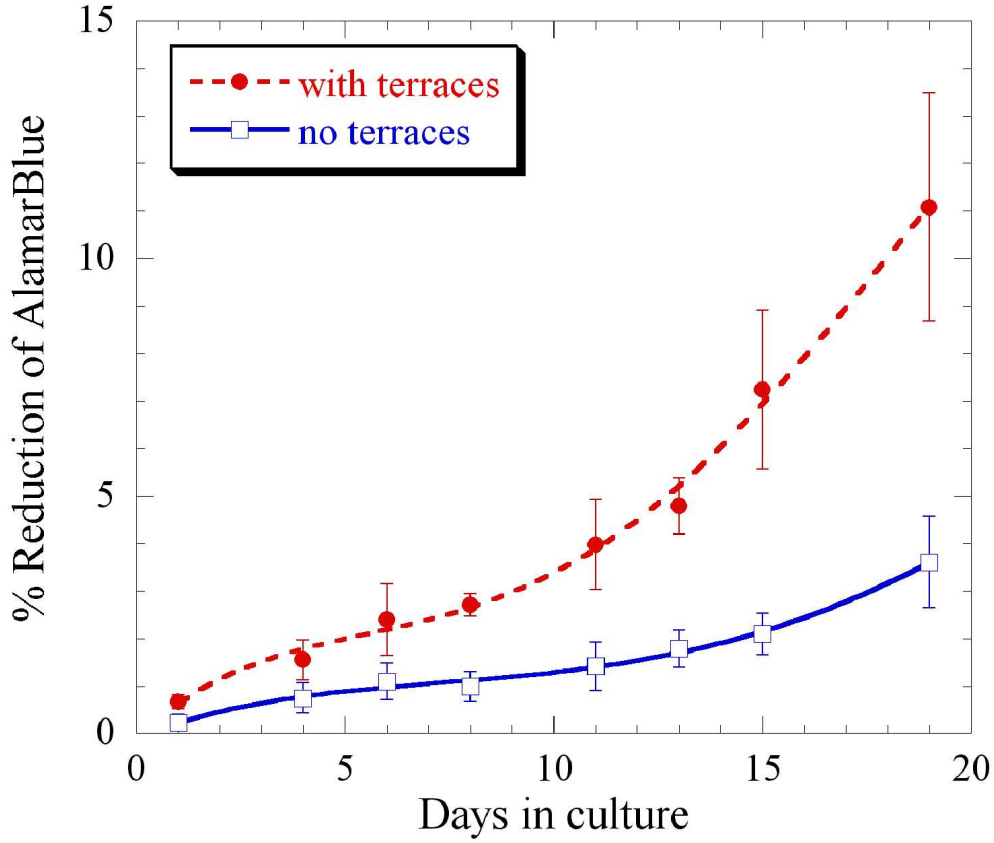

125x107mm (300 x 300 DPI)

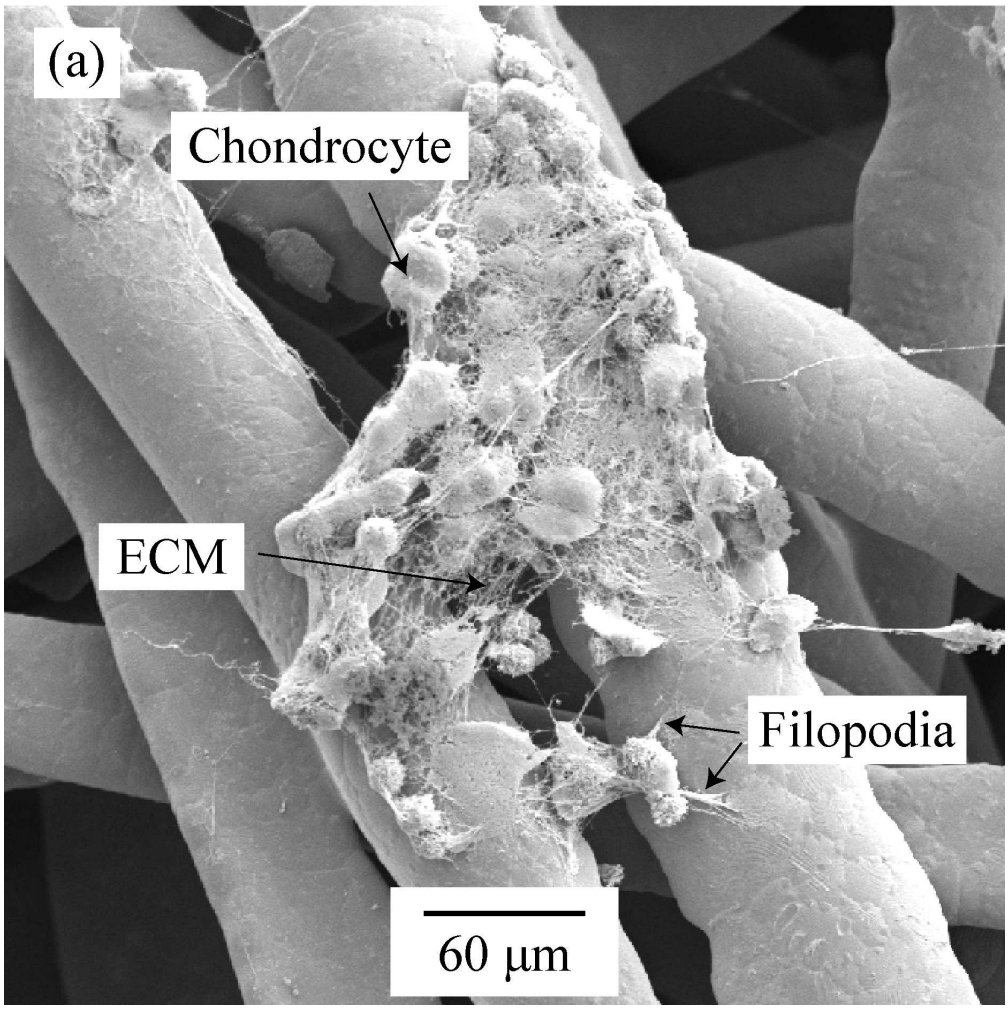

158x158mm (300 x 300 DPI)

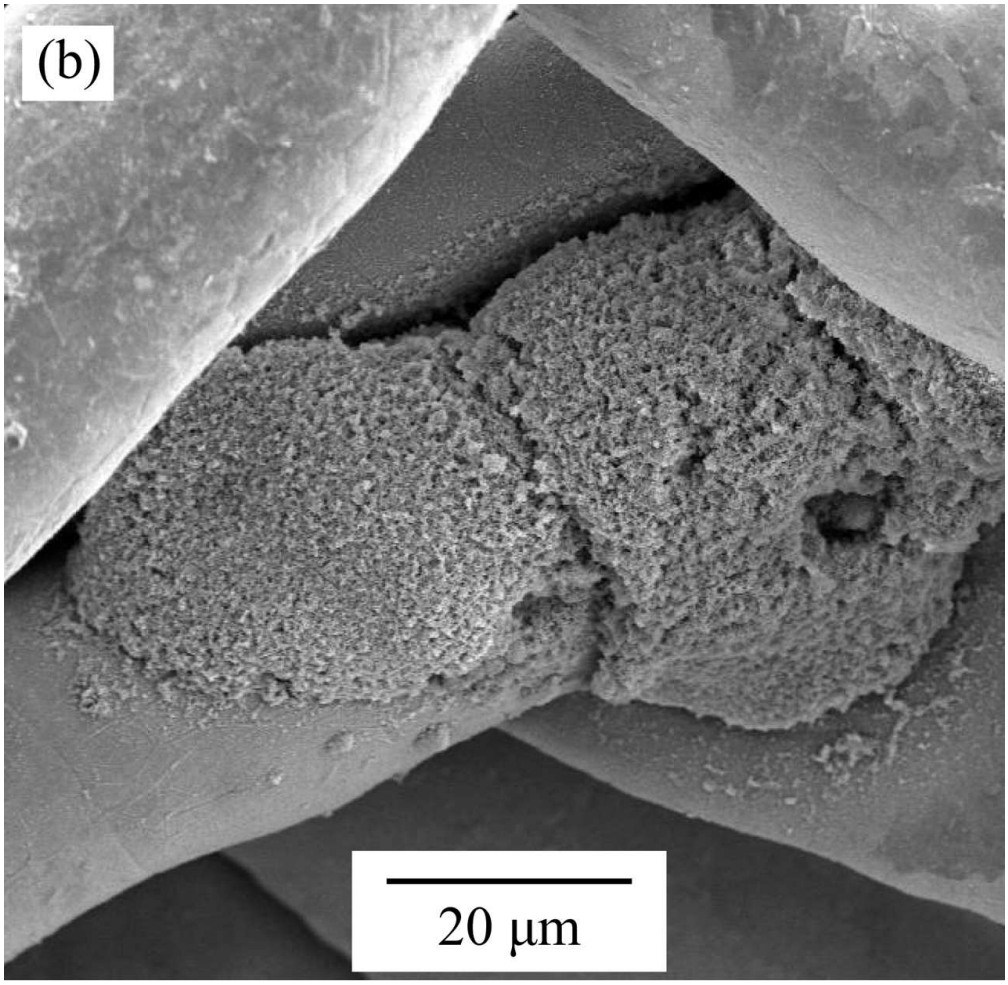

108x105mm (300 x 300 DPI)

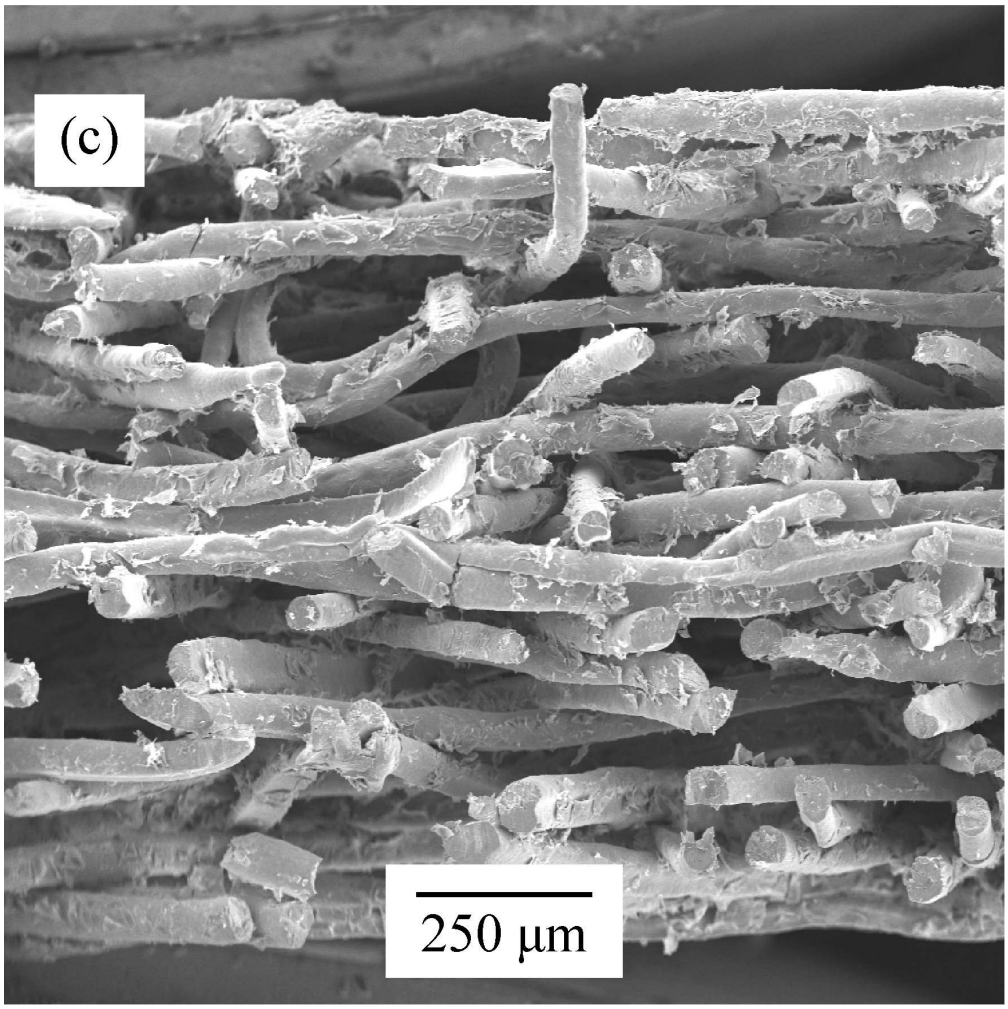

150x150mm (300 x 300 DPI)

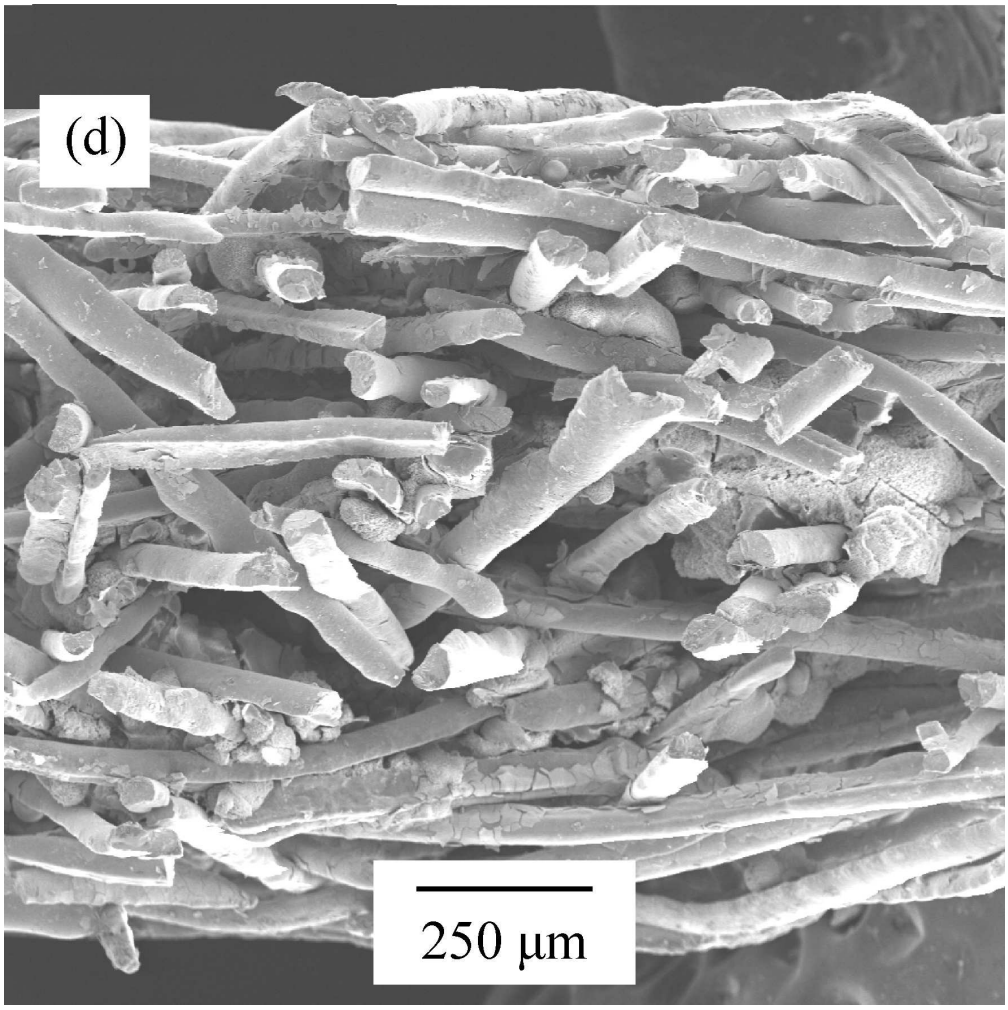

150x150mm (300 x 300 DPI)